Electrical Conductivity and Porosity in Stainless Steel 316L Scaffolds for Electrochemical Devices Fabricated Using Selective Laser Sintering

Khairul Amilin Ibrahim[a,b]* , Billy Wu[c] and Nigel P Brandon[a]

[a] *Department of Earth Science and Engineering, Imperial College London, London SW7 2BP, UK*
[b] *Faculty of Mechanical Engineering, Universiti Teknologi MARA, Shah Alam, 40450 Selangor, Malaysia*
[c] Dyson School of Design Engineering, Imperial College London, London SW7 1NA London, UK

*Corresponding author email address: k.ibrahim14@imperial.ac.uk

ARTICLE INFO

Article history:
Received
Received in revised form
Accepted
Available online

Keywords:
Porous electrode
Laser sintering
Binding mechanism
Electrical conductivity

ABSTRACT

Battery electrode microstructures must be porous, to provide a large active surface area to facilitate fast charge transfer kinetics. In this work, we describe how a novel porous electrode scaffold, made from stainless steel 316L powder can be fabricated using selective laser sintering by proper selection of process parameters. Porosity, electrical conductivity and optical microscopy measurements were used to investigate the properties of fabricated samples. Our results show that a laser energy density between 1.50-2.00 J/mm^2 leads to a partial laser sintering mechanism where the powder particles are partially fused together, resulting in the fabrication of electrode scaffolds with 10% or higher porosity. The sample fabricated using 2.00 J/mm^2 energy density (60W – 1200 mm/s) exhibited a good electrical conductivity of 1.80 x 10^6 S/m with 15.61% of porosity. Moreover, we have observed the porosity changes across height for the sample fabricated at 60W and 600 mm/s, 5.70% from base and increasing to 7.12% and 9.89% for each 2.5 mm height toward the top surface offering graded properties ideal for electrochemical devices, due to the changing thermal boundary conditions. These highly porous electrode scaffolds can be used as an electrode in electrochemical devices, potentially improving energy density and life cycle.

1. Introduction

Selective Laser Sintering (SLS) is an additive manufacturing technology that has grown rapidly, and has a wide application potential because of its flexibility. These advantages have provided a wide platform in areas such as medical research, e.g. to study the process of hydroxyapatite using laser sintering for bone tissue engineering [1], in manufacturing, e.g. in rapid casting [2] and in civil engineering, e.g. in bridge manufacturing [3]. In spite of these advantages, its application to electrochemical device development has been limited to date. One example of its application in this field is the fabrication of three-dimensional (3D) Li-ion microbattery architectures, where the researchers used 3D printing techniques to create interdigitated electrodes from specially developed inks [4].

Electrochemical devices are capable of converting chemical energy to/from electrical energy at very high efficiency. Such devices include the lithium-ion battery, solid-oxide fuel cell and metal-air battery, amongst others. Currently, the development of these devices has become crucial in order to support de-carbonisation targets, for example through battery electric vehicles [5,6]. This development faces many challenges, for instance the need to safely improve battery energy density and cycle life, [7,8,9,10]. Researchers have been working over a decade to solve the problems in metal-air batteries such as life cycle limitation, non-uniform zinc dissolution during charge and discharge cycle [11], morphological changes of the zinc electrode [12] and dendritic growth at the zinc anode [13]. Moreover, degradation of the air electrode and carbonization problems due to the reaction between electrolyte and air can block the pores of air cathode damaging the electrode architecture [14]. However, there remain opportunities to continue to improve the performance and lifetime of electrochemical devices such as batteries and fuel cells devices through better design and manufacture of the electrodes.

Literature studies have shown several approaches to improving the performance of metal-air batteries such as suppressing zinc dendrite growth in an ionic liquid electrolyte containing highly concentrated cationic and anionic zinc complexes [15] and the use of Co_3O_4 nanoparticles that were synthesized on N-doped Vulcan carbon as a hybrid bifunctional electrolcatalyst [16]. Another approach with a particular focus on the anode focused on the production of the electrode as foam [17] or fibrous [18] materials to improve life cycle and energy density. Zhang investigated the performance of the zinc-air system by using solid zinc to produce fibrous zinc anodes. This anode increased the discharge capacity by 38 %, material utilization by 26 % and discharge energy by 49 % compared to the gelled atomized powder zinc anode [18]. In another study, Yan et. al. fabricated a 3D zinc foam electrodes by pulse electro-deposition of zinc on copper. When tested under 250 mA cm^{-2} discharge-charge currents, 100 % depth of discharge was achieved without using any dendrite-suppressing additives. The resulting 3D Zn/Cu foam electrodes remain dendrite free after 10,000 discharge-charge cycles and also demonstrated a good cycling stability where it achieved up to 620 mA h g^{-1} of specific capacity after 9000 discharge-charge cycles in a zinc-nickel system [19]. However, performance gaps remain, meaning that further improvements in the electrode would be beneficial. This could be achieved by the development of a 3D porous electrode using SLS. In this study, the capabilities of SLS to fabricate porous scaffold electrodes have been explored to enhance electrochemical device performance. Scaffold electrodes means a 3D aperiodic structure or non-planar geometries of electrodes that utilize more surface area for chemical reaction to take place [20,21,22].

The aim of the study is to investigate the influence of selected process parameters on the additive manufacturing of 316L stainless steel (SS 316L), with the aim of fabricating porous scaffold parts. Such porosity can improve the active surface area compared to planar electrode structures, increasing electrochemical reaction rates [20,21,22], and also deliver higher mass transfer rates within electrode structures. Having such porous metal parts can lead to increased metal surface area for chemical reaction. Later, other active materials can be deposited between void spaces.

Kamath et. al. demonstrated how to fabricate metal parts with a density of more than 99 % from SS 316L via control of laser power and scanning speed [23]. A comparison study of different powder grades (three different particle size distribution) also has been demonstrated with the aim of fabrication of high density SS 316L parts [24]. Whilst more work has been reported on how to achieve high density parts [25,26], there are few studies that discuss how to achieve such porous parts. Such examples include the work conducted by Cijun et. al. Here they demonstrated the correlation between process parameters (laser scanning speed and energy density) and microstructure (grain size and mechanical properties) of laser sintering for porous bone scaffolds [27]. However, this work focuses on the sintering of ß-tricalcium phosphate bioceramic as the materials for laser sintering, not the SS 316L.

Process parameter selection is the most important component in this study. More than 20 process parameters can be explored, such as laser power, laser spot size, hatch space, size of powder particle and layer thickness. They can be classified into four main categories which are material properties, laser parameters, scanning process parameters and environmental parameters [28]. Other researchers who have looked at the influence of process parameters have found that each has influence on specific properties. Kamath et al. highlighted the influence of scan speed followed by laser power on the density of metal parts [23]. In another study, Simchi and Pohl concluded that the density of built parts was an exponential function of the specific energy input of the laser; where a specific energy input is defined as laser power divided by scanning speed and sintered area [29]. Additionally, Noriko et. al. reported the major influence on the SLS build arising from the interaction between laser power, scan speed and scan spacing [30]. From the literature studies, it was concluded that laser power and scan speed are the crucial parameters in determining the porosity of the fabricated parts.

This study includes analysis of the relationship between the laser power, scan speed and energy density on the electrical conductivity of fabricated structures, such conductivity being a pre-requisite for electrochemical device applications. There are two types of porosity to take into consideration when producing scaffold structures. The first is the designed porosity, i.e. the porosity intrinsic to the scaffold design. This is a relatively large length scale, typically 10^{-3} m. The second is the internal porosity of metal parts that make up the structure, typically of the order of 10^{-6} to 10^{-4} m. This internal porosity is generated as a result of the parameters used during the SLS process. In this study we focus only the second form of porosity.

2. Experimental methods

A SS 316L powder, average particle size of 25 to 50 µm and standard chemical composition as supplied by Concept Laser was used in this study. A Concept Laser Mlab Cusing with a laser spot size of approximately 25 µm was used to fabricate samples.

A set of 25 cylindrical samples, of diameter 4 mm and 10 mm in height, each fabricated using a different range of laser powers (30 W to 90 W) and scan speeds (300 mm/s to 1500 mm/s) were produced. Both parameters are correlated, as shown in Eqn. 1 [1].

$$\text{Energy density}\left[\frac{J}{mm^2}\right] = \frac{\text{Laser Power [W]}}{\text{Scan Speed}\left[\frac{\text{mm}}{\text{sec}}\right] \text{x Spot size [mm]}} \qquad \textit{Eqn. 1.}$$

The range of parameters used in the build were set in a matrix form as shown in the Table 1 together with the corresponding energy density. For the purposes of sample identification, they were labelled as laser power-scan speed (e.g. sample 30-1500 means that the sample was built using a laser power of 30 W and a scan speed of 1500 mm/s).

Table 1
Matrix of parameter selection, showing the variation in energy density with laser power and scan speed.

		Laser Power (W)				
		30	**45**	**60**	**75**	**90**
Scan Speed (mm/sec)	**300**	4.00	6.00	8.00	10.00	12.00
	600	2.00	3.00	4.00	5.00	6.00
	900	1.33	2.00	2.67	3.33	4.00
	1200	1.00	1.50	2.00	2.50	3.00
	1500	0.80	1.20	1.60	2.00	2.40

* Energy density is shown in unit of J/mm^2

The array of samples on the build plate is shown in Fig. 1. The red arrow to the right represents the increment in laser power (from low to high) while the green arrow in the downward direction represents the increment in scan speed (from low to high). As shown, samples were arranged in a wave pattern. This is to avoid a non-uniform metal powder spread when the distance, d, is too close.

A systematic analysis was performed, including: 1) optical microscopy analysis on the surface of samples; 2) bulk porosity measurement; and 3) electrical conductivity measurement for each sample to investigate the effect of the laser parameters on the properties of the fabricated metal parts.

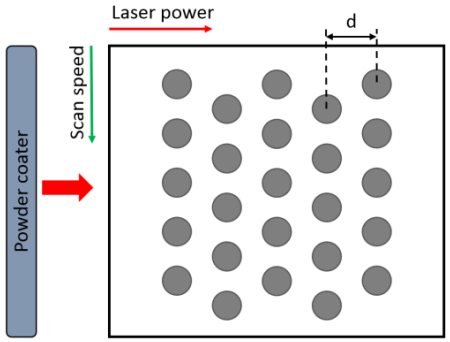

Fig. 1. Array of 25 samples on the build plate based on the matrix in Table 1.

The density of samples was calculated based on the measured volume and mass. Mass was measured on an electronic balance to an accuracy of ±0.0001 g. A digital Vernier caliper (accurate to ±0.01mm) was used to measure the diameter and height of samples. Samples were assumed to be cylindrical, though it was observed that some of samples had a shrinkage defect on their top surface. The porosity value was determined by subtracting the

measured density value from the literature density value for stainless steel 316L (8.0 g/cm^3 [31]).

The measurements of conductivity were based on the Van der Pauw method [32,33,34], which is widely used in determining the conductivity of materials. In this experiment, an Autolab PGSTAT302N potentiostat was used to provide the source of current and to measure the voltage across the samples.

For the optical microscopy analysis, surfaces of samples were ground, polished and etched using glyceregia (3 parts hydrochloric acid, 2 parts glycerol and 1 part nitric acid) to highlight the grain structure before examination by optical microscopy. Due to the small sample size, a Bakelite Phenolic mounting resin was used to mount the samples to hold it during the grinding and polishing process. After etching for 5 minutes, the surface of the samples were observed using the Olympus optical microscope, BX51.

3. Results

Initially, 25 samples were set-up to be fabricated using SLS. However, it was noted that only 24 samples were successfully printed. The sample produced using a laser power of 30 W, scan speed of 1500 mm/s and an energy density of 0.80 J/mm^2, could not be produced. The reason for this was the combination of low laser power and fast scan speed, which resulted in insufficient time for the laser beam to deliver enough thermal energy to melt and fuse the metal powder together. Interestingly, although sample 30-1500 was not successfully printed as a solid cylinder, there was an evidence of its fabrication from the shell chip that was left after the SLS. The result indicates that a laser re-melting process occurred during the laser sintering process.

Laser re-melting is a process where a second laser scan is applied to the same slice before spreading a new layer of metal powder. It has the advantages of improving both the surface quality and the density of metal parts [35]. Evidence of the effect of the laser re-melting was found by Yasa and Kruth; they demonstrated that laser re-melting increased the density of SLS parts to approximately 100 % and enhanced the surface roughness to make it smoother by about 90 % [36].

All samples underwent a laser re-melting procedure on the inner and outer contour after fabrication. The outer contour refers to a re-melting process (second laser scan) at the outer boundary of the circular geometry over the full height of metal part, while inner contour refers to a re-melting process on the top surface as illustrated in the Fig. 2.

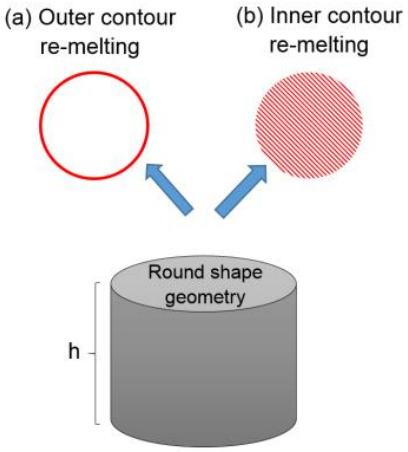

Fig. 2. Laser re-melting process (a) Outer contour laser scan at the outer surface of the sample, (b) Inner contour laser scan on the top surface.

Although laser re-melting can increase densification of the printed part, it also can cause shrinkage defects due to the high thermal energy that is delivered to the surface of the layer. This phenomenon was clearly observed on a few samples, as shown in Fig. 3.

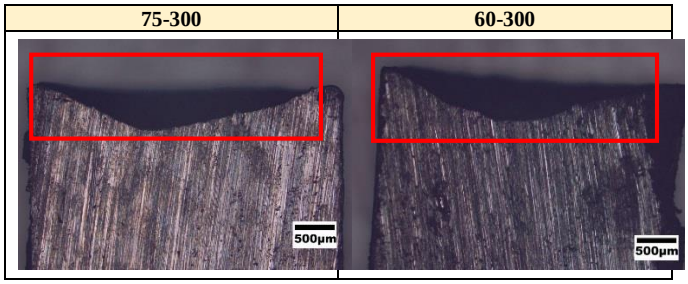

Fig. 3. Cross section of the 75-300 and 60-300 samples, showing a shrinkage defect on the top surface using an optical microscope.

Table 2
Bulk density and porosity for 24 samples of SS 316L based on the matrix in Table 1.

Scan Speed (mm/s)		Laser Power (W)									
		30		45		60		75		90	
		Range	Average	Range	Average	Range	Average	Range	Average	Range	Average
300	Bulk density (g/cm^3)	7.02-7.11	7.07	7.45-7.54	7.50	7.41-7.50	7.46	7.30-7.39	7.34	7.32-7.41	7.36
	Bulk porosity (%)	11.11-12.19	11.65	5.70-6.85	6.27	6.21-7.35	6.78	7.66-8.78	8.22	7.38-8.50	7.94
600	Bulk density (g/cm^3)	6.24-6.32	6.28	7.19-7.28	7.23	7.38-7.47	7.43	7.55-7.64	7.59	7.46-7.55	7.50
	Bulk porosity (%)	20.99-21.96	21.48	9.02-10.13	9.57	6.60-7.73	7.16	4.49-5.65	5.07	5.65-6.79	6.22
900	Bulk density (g/cm^3)	5.55-5.62	5.58	6.58-6.66	6.62	7.20-7.29	7.25	7.60-7.70	7.65	7.59-7.69	7.64
	Bulk porosity (%)	29.80-30.68	30.24	16.76-17.78	17.27	8.84-9.95	9.40	3.80-4.97	4.38	3.94-5.11	4.52
1200	Bulk density (g/cm^3)	4.92-4.98	4.95	6.01-6.09	6.05	6.71-6.79	6.75	7.40-7.49	7.45	7.55-7.65	7.60
	Bulk porosity (%)	37.73-38.52	38.13	23.92-24.85	24.39	15.09-16.13	15.61	6.34-7.48	6.91	4.44-5.60	5.02
1500	Bulk density (g/cm^3)	-	-	5.63-5.70	5.66	6.29-6.37	6.33	6.95-7.04	6.99	7.32-7.41	7.36
	Bulk porosity (%)	-	-	28.79-29.67	29.23	20.36-21.34	20.85	12.04-13.12	12.58	7.42-8.55	7.98

3.1 Density and porosity measurements

The measured density and porosity values are tabulated in Table 2, along with the range of uncertainty determined by error propagation.

Several observations can be made on the trend of porosity of samples for different sets of laser power and scan speed. The results obtained from Table 2 are shown in Fig. 4. It is apparent in Fig. 4-a that, at constant scan speed, the porosity of samples decreased as the laser power increased, whereas for samples fabricated using scan speeds of 300 mm/s and 600 mm/s, the porosity started to increase after the laser power reach 45 W and 75 W. A higher sensitivity of porosity to laser power was observed for samples fabricated using a scan speed of 1500 mm/s compared to the scan speed of 300 mm/s.

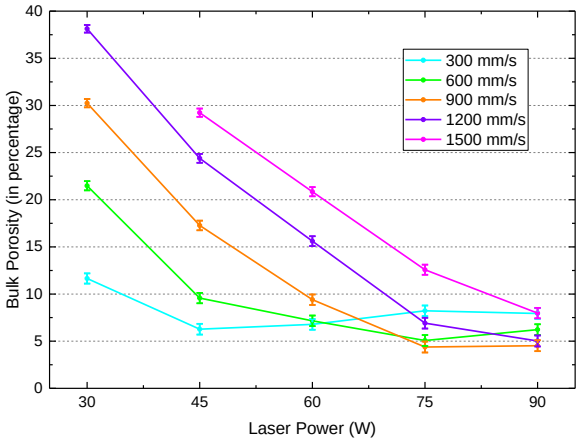

[a]

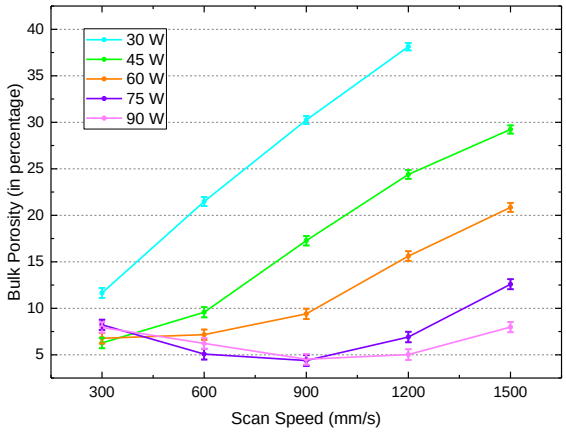

[b]

Fig. 4. Trend of porosity for different sets of laser power and scan speed. [a]- Bulk porosity (with error bar) of SS 316L samples versus Laser Power at constant scan speed. [b]- Bulk porosity (with error bar) of SS 316L versus Scan Speed at constant laser power.

As can be seen in Fig. 4-b, increasing scan speed resulted in an increase of porosity when a constant value of laser power was used. However, a different trend of porosity was shown for the laser power of 75 W and 90 W. At first, the porosity of samples decreased as scan speed increased. When it reaches a scan speed of 900 mm/s, the porosity started to rise proportional with the increase in scan speed. Fig. 4-b also shows that the rate of change of porosity with the scan speed is greater as laser power decreases, over the range tested here.

In order to have a better understanding of the relationship between laser power and scan speed, the effect of energy density on the porosity of samples was analysed. The results, shown in Fig. 5 indicates that the highest porosity was observed at a laser energy density of 1.00 J/mm^2 while the lowest porosity was observed at the laser energy density of 3.33 J/mm^2. There is a clear trend of decreasing porosity as energy density increased. This result was supported by the study conducted by Cherry et. al.; who found that porosity was low at high energy density and increased as laser energy density decreases [37]. Interestingly, porosity starts to increase when energy density is 5.00 J/mm^2 and higher, due to powder ablation. Noriko et. al. observed the same trend using a different material, namely a A1Si10Mg alloy. They concluded that the porosity increase above a critical energy density was caused by vapourisation [30].

The graph in Fig. 5 was divided into 3 main regions; *Region 1* for the range of energy densities between 1.00 to 2.00 J/mm^2 which shows that the porosity tends to drop off quickly as energy density increases; *Region 2* is for energy densities between 2.01 to 4.00 J/mm^2 and shows a wider distribution of porosity as the energy density increases; whereas in *Region 3*, where energy density above 4.01 J/mm^2, the porosity slowly increases as energy density increases.

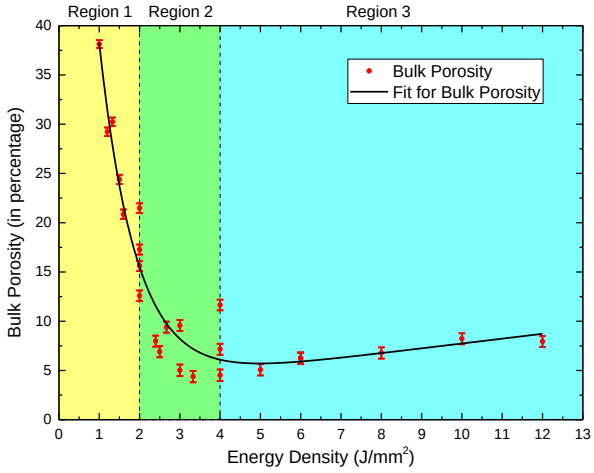

Fig. 5. Bulk porosity (with error bar) for 24 samples of SS 316L for energy density in the range of 1.00 to 12.00 J/mm^2.

The data plotted in region 1 shows that here the sintering process is significantly influenced by the laser sintering duration, while in region 2 the sintering process is significantly influenced by the laser power. However, for region 3, the sintering process is dominated by laser ablation, i.e. the laser energy density is sufficient to cause material removal.

3.2 Electrical conductivity

The results obtained from the conductivity measurements are presented in Fig. 6 From the graph (see Fig. 6-a), it can be seen that the conductivity decreased as scan speed increased at a given value of laser power from 30 W to 75 W, with a maximum in the conductivity-laser power curve at lower scan speeds.

The trend in conductivity with laser power is mainly due to the associated changes in sample porosity. As the porosity increased, the conductivity decreased. This relationship is clearly shown in Fig. 4 and Fig. 6; low laser power or high scan speed produced high porosity, decreasing conductivity.

This finding is further supported by Fig. 7. It is apparent that conductivity decreases as bulk porosity increases. However, for a bulk porosity of less than 15 %, results show a non-linear pattern in conductivity against bulk porosity, suggesting that it is not just the porosity that affects the conductivity, but also how the particles

are sintered together. This will be discussed further in the next section.

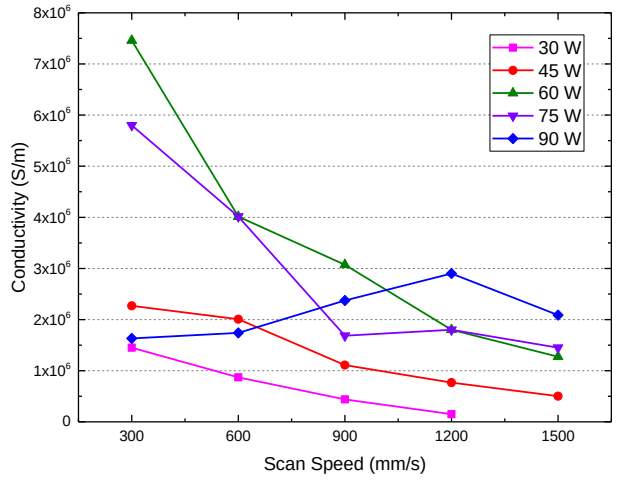

[a]

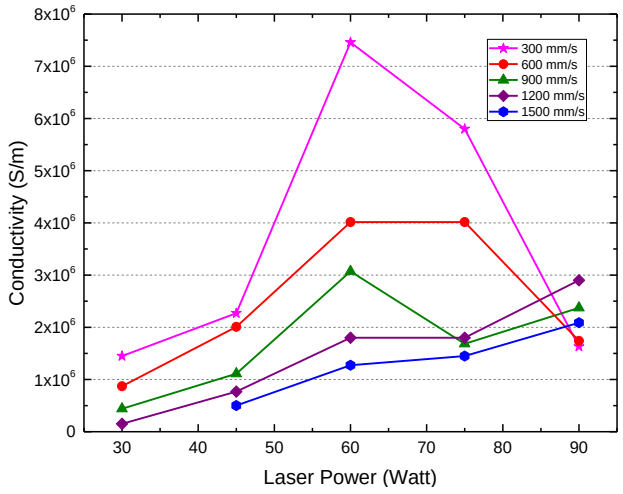

[b]

Fig. 6. Trend of conductivity for different sets of scan speed and laser power. [a]- Conductivity against scan speed at various constant laser power. [b]- Conductivity against laser power at various constant scan speeds.

3.3 Optical microscopy analysis

Finally, the study observed the influence of laser parameters on the microstructure of the samples. For this analysis, sample 60-600 was chosen from the high porosity group samples. This was cut into 4 sections across the sample height (see Fig. 8). The surfaces of sub-samples 2, 3 and 4 were ground, polished and etched as previously prescribed in the section 2.

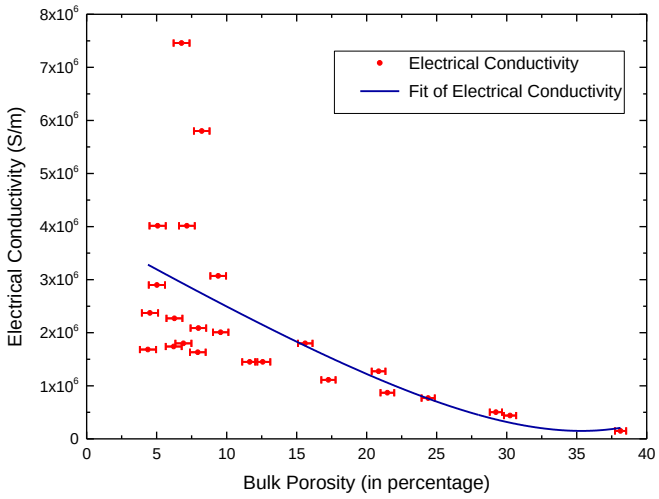

Fig. 7. Trend of electrical conductivity for 24 samples with various bulk porosity (with error bar) in the range of 4.38% to 38.13%.

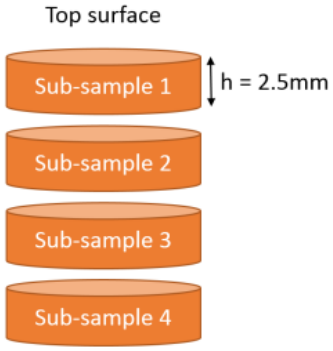

Fig. 8. Sample 60-600 was cut into four sections across its height.

It was observed that porosity varied with location in the original sample (Fig. 9). The distribution of the porosity was clearly not uniform. The porosity for each sub-samples was then determined using the Image J software. It was found that the porosity of the sample was higher at the base. From this result, it could be concluded that the porosity of the sample decreased with build height, from the base to the top. The average porosity value from the image analysis was 7.57 %. Previously, the porosity for the sample 60-600 was measured at 7.16 %.

Sub-sample 2	Sub-sample 3	Sub-sample 4
	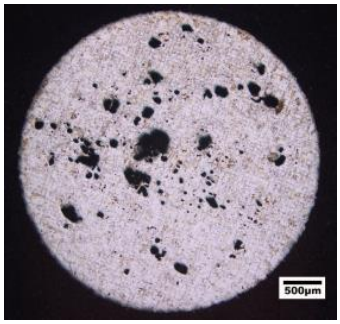	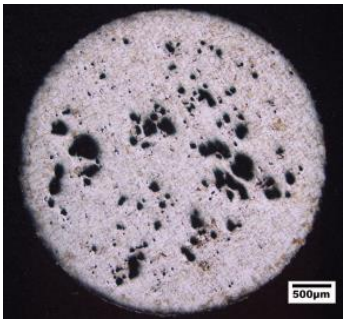
Porosity 5.70 %	Porosity 7.12 %	Porosity 9.89 %

Fig. 9. Optical microscopy images for 3 sub-samples after the etching process at the magnification of 2.5X.

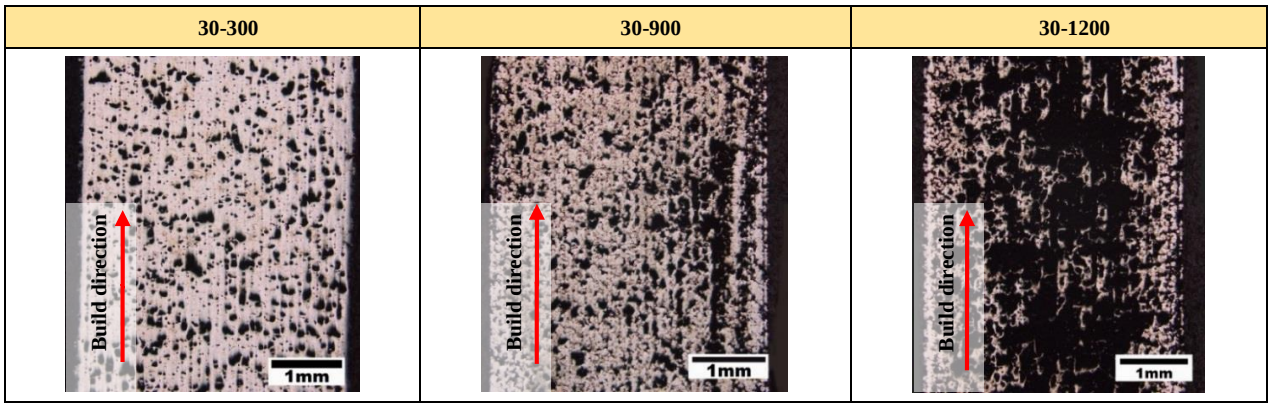

Fig. 10. Pores distribution in samples printed using a laser power of 30 W, various laser scan speed.

Next, three samples that had high porosity values were cut symmetrically in a vertical direction, and observed by optical microscopy. All samples were built using a laser power of 30 W, but at various scan speeds. The images are shown in Fig. 10. It was found that the porosity of the samples changed with build height, as previously observed for sample 60-600. A non-uniform pore distribution can be seen within the samples, for three different locations at the same laser scan rates. The porosity is higher at low build heights, reducing throughout the process. This phenomenon can be attributed to a temperature gradient between each layer due to thermal conduction.

In this case, the thermal conduction phenomenon during SLS is illustrated in Fig. 11. The top surface of each slice will experience high temperatures when absorbing the thermal energy during the laser scan; heat then will transfer to the base plate through the metal support due to the imposed thermal gradient. The process continues, more slices are added and sintered and will cause the conduction distance, d for the heat conduction to increase. The longer travelling distance can increase the thermal resistance, leading to a higher transfer period, thus reducing the rate of heat transfer [38]. Low rates of heat transfer means the thermal energy will be stored for longer periods, providing sufficient heat to completely melt and fuse metal powders, thus reducing the porosity.

The surfaces of the sub-samples of sample 60-600 were then observed at higher magnification (50X) as shown in Fig. 12; these images reveal the grain structures of the cross-section of the sub-samples. The same fine cellular grain structure was observed in all images. This means that no grain structural changes were evident across the height of the samples. This grain structure is formed due to the high cooling rates encountered in the laser sintering process, resulting in rapid solidification, and are representative of those commonly obtained by the SLS process [36].

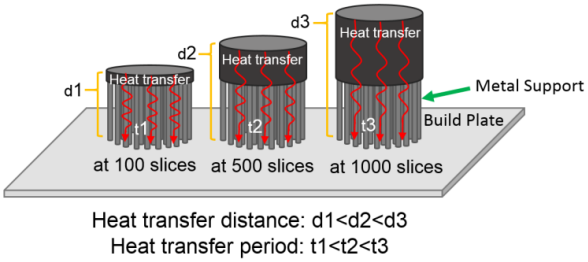

Fig. 11. Schematic illustration of thermal conduction during SLS.

Further observation was conducted to identify two structures in these images; the light region is ferrite while the dark region is pearlite. Pearlite is the eutectoid structure that forms by the simultaneous precipitation of ferrite and cementite at the eutectoid temperature.

Further investigation was conducted to investigate the influence of the microstructure on the conductivity of samples. It was found that the metal sintering conditions influenced the conductivity. As previously reported by Zhu et. al, a lower energy density resulted in the formation of voids in the sample while higher energy densities resulted in a more dense sample [39]. This would be expected to influence the electrical conductivity. Fig. 13 shows the optical microscopy images of the microstructures for samples with low, medium and high conductivity. The image for sample 90-900 (high conductivity) shows that the powder particles were fully melted and fused together, while the image for sample 45-1500 (low conductivity) shows that the powder particles were only partially melted and fused together. Interestingly, the image for sample 30-1200 shows that some of the powder particles were partially melted while some were not melted (shown by the red circle). The un-melted powder particles have a clear boundary region. Hence, this could explain why this sample has a lower conductivity.

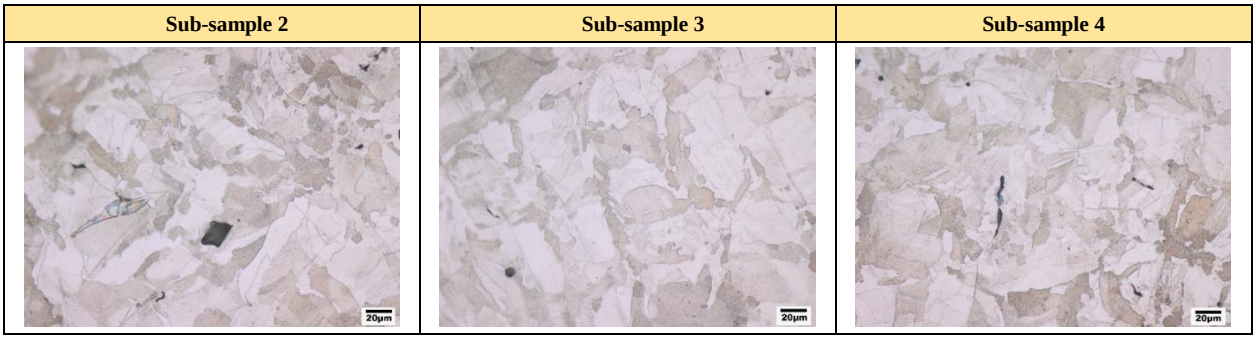

Fig. 12. Images of microstructure for sample 60-600 at 3 different height locations at a magnification of 50X

Sample 90-900	Sample 45-1500	Sample 30-1200
		
(σ = 2.37x10^6 S/m)	(σ = 0.50x10^6 S/m)	(σ = 0.15x10^6 S/m)

Fig. 13. Comparison of microscopy images of the microstructure for different samples highlighting the influence of particle sintering on the electrical conductivity.

4. Discussion

This study set out with the aim of assessing the influence of the SLS process parameters on the properties and microstructure of printed parts, with a focus on determining the process parameters that enable fabrication of porous structures. 24 samples were successfully printed using SLS. Sample 30-1500 was not produced because there was not enough laser energy to heat the powder particles due to the low ratio between laser power and scan speeds. Laser re-melting (outer contour and inner contour parameters) were used in this study so that sample shell strength could be improved, better surface quality achieved, while at the same time retaining a high internal porosity. This result agrees with the findings of other studies, in which laser re-melting can improve the density and enhance the surface roughness of printed parts [35,40,41]. From these findings, the high porosity parts, which were generally printed using an energy density less than 2.00 J/mm^2, might not print well if their shells were too weak.

Another important finding was that the porosity is high at low laser power and high scan speed. This is consistent with other studies, and suggests that low laser power and high scan speed produce low density parts [29, 42, 43]. The lowest density part, which exhibited a porosity of 38.13 %, was fabricated by using a laser power of 30W and scan speed of 1200 mm/s. However, this high percentage of porosity will certainly reduce the mechanical strength as previously reported [44]. Sercombe et. al [45] have also shown that mechanical strength can be related to the materials relative density, properties and either open or closed porosity forms. However, it should be noted that the aim of this study was to fabricate highly porous metal parts, to be used as an electrode in any electrochemical devices. Hence the mechanical properties were not a crucial factor in this case, as long as the shape could be retained.

It is also difficult to choose the right combination value of both parameters without establishing the relationship between them. The present findings suggest that energy density is a good parameter when selecting processing conditions. In accordance with the previous studies, this work has demonstrated that, at low energy density, the porosity is found to be high, reducing when the energy density is increased until a point of minimum porosity is reached (in this study approximately at 5.00 J/mm^2), after which the porosity start to increase again with energy density due to the ablation of material [36]. Samples that were fabricated with an energy density more than 4.00 J/mm^2 experience shrinkage defect and material ablation. Amongst them, sample 90-300, which was fabricated with an energy density of 12.00 J/mm^2 exhibit the highest material ablation. This phenomenon explains the result observed in the Table 1 showing that the highest density of metal parts of 95.48 % was fabricated using a lower energy density of 4.00 J/mm^2.

This study found that the electrical conductivity reduced with porosity, as previously reported [46,47]. The highest electrical conductivity of 7.45 x 10^6 S/m was measured for sample 60-300, which is not the lowest measured porosity value. This result shows that it is not just the porosity that influences conductivity. A non-linear change in conductivity with porosity was observed, suggesting that it is not just the internal volume that affects the conductivity of samples but also how well the particles sinter together, with poor particle-to-particle sintering being an additional source of resistance in the samples, as illustrated in Fig. 14. This means that if two samples have the same porosity, the conductivity can vary depending on the particle-to-particle interfaces and distribution of voids. A non-uniform void distribution can cause more tortuous conduction paths, lowering conductivity. In addition, the void distribution was found to be influenced by the type of laser sintering. Specifically, partial sintering tends to produce non-uniform void distribution. Hence it can be concluded that partial sintering also contributed to the differences in conductivity of samples.

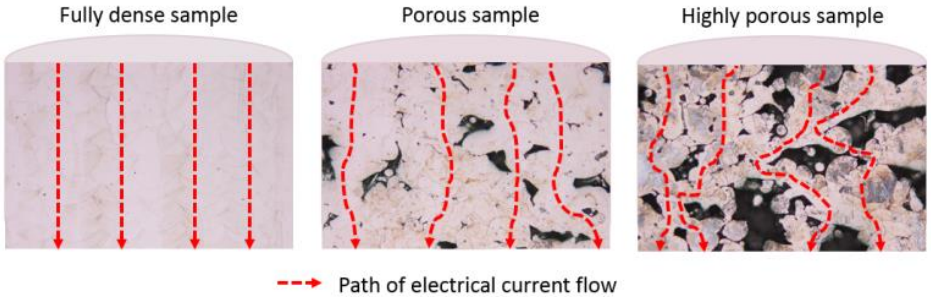

Fig. 14. Illustration of the porosity effect on the electrical conductivity of samples. Higher porosity leads to more tortuous conductions paths.

Observation of the cross section of the sintered parts gave insight into the fabrication process. Two mechanisms for metal powder sintering were observed in this study;

1- the powder particles were partially melted, thus the powder particle partially fused together, forming the sintering necks observed in Fig. 13 (sample 45-1500).
2- the powder particles were completely melted, fusing together into a homogenous part as observed in Fig. 13 (sample 90-900).

These binding mechanism are schematically illustrated in Fig. 15.

The actual mechanism depends on the amount of heat transferred to the surface of the layer and its operating temperature. In other words, the more energy transferred to the surface and the higher the temperature the more likely that dense parts will be obtained. These results match those observed in earlier studies. Kruth et al. observed the same condition where, by fully melting the powder particles, a high density could be achieved [48]. Tolochko et al. concludes that laser sintering consists of two binding mechanisms as stated above [49].

It is interesting to observe that porosity varies along the build height of samples. This finding was unexpected and suggests that the porosity of samples are higher at the base, reducing towards the top surface. A possible explanation for this can be caused by the thermal gradient and heat conduction as previously explained. This grading of the porosity is a further advantage for electrochemical systems as shown by a number of modelling studies [50,51].

Conclusions

This work shows that it is possible to select the correct process parameters in SLS to produce porous metal sintered parts that could form the basis of a scaffold electrode for electrochemical, and other devices. These findings suggest that high porosity metal parts can be produced by using a low laser power and high scan speed, though there is a minimum laser power and maximum scan speed, outside of which they cannot be successfully printed. Energy density represents the combination of these two parameters. Based on these studies, for the powders used here, a high porosity (more than 10 %) samples can be printed by using an energy density in the range of 1.50 to 2.00 J/mm^2.

It is also concluded that the fabrication conditions that result in partial melting of the powder particles should be used in order to produce high porosity metal parts. A significant finding to emerge from this study is that the electrical conductivity is also influenced by the particle powder boundary resistance. Un-melted or partially melted powder particles result in lower electrical conductivity. This finding shows the need to find a balance between the targeted porosity values, the mechanical integrity of the sample, and the required electrical conductivity.

Finally, the sample fabricated using 60 W laser power, 1200 mm/s scan speed and 2.00 J/mm^2 energy density, having a porosity of 15.61 % exhibited good electrical conductivity of 1.80 x 10^6 S/m.

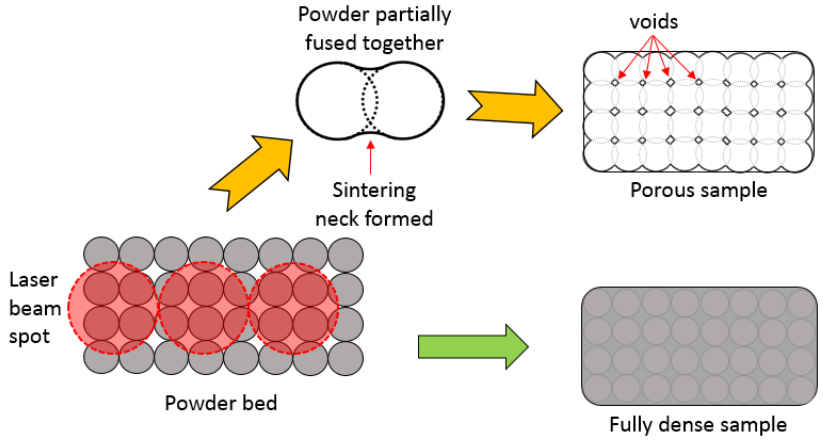

Fig. 15. Schematic illustration of binding mechanisms where powder particles develop a sintering neck to form a porous sample, or melt to form a dense sample.

Acknowledgments

We would like to thank for the financial support for this research from the MARA University of Technology, Malaysia under scholarship SLAB/SLAI in part by the Ministry of Higher Education, Malaysia. This work was also supported by the EPSRC capital grant for Energy storage for low carbon grids (EP/J021199/1) and EPSRC capital grant for medical robotics (EP/J021199/1).

References

[1] C. Shuai, P. Feng, C. Cao, and S. Peng, "Processing and characterization of laser sintered hydroxyapatite scaffold for tissue engineering," *Biotechnol. Bioprocess Eng.*, vol. 18, no. 3, pp. 520–527, 2013.

[2] E. Bassoli, A. Gatto, L. Iuliano, and M. G. Violante, "3D printing technique applied to rapid casting," *Rapid Prototyp. J.*, vol. 13, no. 3, pp. 148–155, 2007.

[3] B. Berman, "3-D printing: The new industrial revolution," *Bus. Horiz.*, vol. 55, no. 2, pp. 155–162, 2012.

[4] K. Sun, T. S. Wei, B. Y. Ahn, J. Y. Seo, S. J. Dillon, and J. A. Lewis, "3D printing of interdigitated Li-ion microbattery architectures," *Adv. Mater.*, vol. 25, no. 33, pp. 4539–4543, 2013.

[5] X. Yuan, X. Liu, and J. Zuo, "The development of new energy vehicles for a sustainable future: A review," *Renew. Sustain. Energy Rev.*, vol. 42, pp. 298–305, 2015.

[6] B. Diouf and R. Pode, "Potential of lithium-ion batteries in renewable energy," *Renew. Energy*, vol. 76, pp. 375–380, 2015.

[7] Z. Ma, X. Yuan, L. Li, Z.-F. Ma, D. P. Wilkinson, L. Zhang, and J. Zhang, "A review of cathode materials and structures for rechargeable lithium-air batteries," *Energy Environ. Sci.*, vol. 8, no. 8, pp. 2144–2198, 2015.

[8] L. Grande, E. Paillard, J. Hassoun, J. B. Park, Y. J. Lee, Y. K. Sun, S. Passerini, and B. Scrosati, "The lithium/air battery: Still an emerging system or a practical reality?," *Adv. Mater.*, pp. 784–800, 2014.

[9] F. Cheng, J. Liang, Z. Tao, and J. Chen, "Functional materials for

rechargeable batteries," *Adv. Mater.*, vol. 23, no. 94, pp. 1695–1715, 2011.

[10] N. Nitta, F. Wu, J. T. Lee, and G. Yushin, "Li-ion battery materials: Present and future," *Mater. Today*, vol. 18, no. 5, pp. 252–264, 2015.

[11] M. A. Rahman, X. Wang, and C. Wen, "High Energy Density Metal-Air Batteries: A Review," *J. Electrochem. Soc.*, vol. 160, no. 10, pp. A1759–A1771, 2013.

[12] K. Wang, P. Pei, Z. Ma, H. Xu, P. Li, and X. Wang, "Morphology control of zinc regeneration for zinc-air fuel cell and batter," *J. Power Sources*, vol. 271, pp. 65–75, 2014.

[13] P. Pei, K. Wang, and Z. Ma, "Technologies for extending zinc-air battery's cyclelife: A review," *Appl. Energy*, vol. 128, pp. 315–324, 2014.

[14] J. S. Lee, S. T. Kim, R. Cao, N. S. Choi, M. Liu, K. T. Lee, and J. Cho, "Metal-air batteries with high energy density: Li-air versus Zn-air," *Adv. Energy Mater.*, vol. 1, pp. 34–50, 2011.

[15] Z. Liu, G. Pulletikurthi, A. Lahiri, T. Cui, and F. Endres, "Suppressing the dendritic growth of zinc in an ionic liquid containing cationic and anionic zinc complexes for battery applications," *Dalt. Trans.*, 2016.

[16] T. An, X. Ge, T. S. A. Hor, F. W. T. Goh, D. Geng, G. Du, Y. Zhan, Z. Liu, and Y. Zong, "Co 3 O 4 nanoparticles grown on N-doped Vulcan carbon as a scalable bifunctional electrocatalyst for rechargeable zinc–air batteries," *RSC Adv.*, vol. 5, no. 92, pp. 75773–75780, 2015.

[17] J.-F. Drilleta, M. Adamb, S. Bargb, A. Herterc, D. Kochd, V. S. And, and M. Wilhelmf, "Development of a Novel Zinc/Air Fuel Cell with a Zn Foam Anode, a PVA/KOH Membrane and a MnO2/SiOC-Based Air Cathode," *ECS Electrochem. Soc.*, vol. 28, no. 32, pp. 13–24, 2010.

[18] X. G. Zhang, "Fibrous zinc anodes for high power batteries," *J. Power Sources*, vol. 163, no. September, pp. 591–597, 2006.

[19] Z. Yan, E. Wang, L. Jiang, and G. Sun, "Superior cycling stability and high rate capability of three-dimensional Zn/Cu foam electrodes for zinc-based alkaline batteries," *RSC Adv.*, vol. 5, pp. 83781–83787, 2015.

[20] T. S. Arthur, D. J. Bates, N. Cirigliano, D. C. Johnson, P. Malati, J. M. Mosby, E. Perre, M. T. Rawls, A. L. Prieto, and B. Dunn, "Three-dimensional electrodes and battery architectures," *MRS Bulletin*, vol. 36, no. 07. 2011 Materials Research Society, pp. 523–531, 2011.

[21] B. Dunn, C. J. Kim, and S. Tolbert, "Three-dimensional microbatteries for MEMS/NEMS technology," *Proc. IEEE Int. Conf. Micro Electro Mech. Syst.*, pp. 164–167, 2010.

[22] J. W. Long, B. Dunn, D. R. Rolison, and H. S. White, "Three-dimensional battery architectures," *Chem. Rev.*, vol. 104, no. 10, pp. 4463–4492, 2004.

[23] C. Kamath, G. F. Gallegos, and A. Sisto, "Density of Additively-Manufactured , 316L SS Parts Using Laser Powder-Bed Fusion at Powers Up to 400W," *Lawrence Livermore Natl. Lab.*, vol. LLNL-TR-64, pp. 1–19, 2013.

[24] G. L. A. B. Spierings, "Comparison of Density of Stainless Steel 316L parts produced with Selective Laser Melting using Different Powder Grades," *SFF Symp. 2009*, pp. 1–12, 2009.

[25] J. Delgado, J. Ciurana, and C. A. Rodríguez, "Influence of process parameters on part quality and mechanical properties for DMLS and SLM with iron-based materials," *Int. J. Adv. Manuf. Technol.*, vol. 60, no. 5–8, pp. 601–610, 2012.

[26] M. Rosso and M. A. Grande, "High density sintered stainless steels with improved properties," vol. 21, no. 2, pp. 97–102, 2007.

[27] C. Shuai, P. Feng, L. Zhang, C. Gao, H. Hu, S. Peng, and A. Min, "Correlation between properties and microstructure of laser sintered porous β -tricalcium phosphate bone scaffolds," *Sci. Technol. Adv. Mater.*, vol. 14, no. April, p. 055002, 2013.

[28] M. Król, M. Kujawa, L. A. Dobrzański, and T. Tański, "Influence of technological parameters on additive manufacturing steel parts in Selective Laser Sintering," *Int. Sci. J.*, vol. 67, no. 2, pp. 84–92, 2014.

[29] A. Simchi and H. Pohl, "Effects of laser sintering processing parameters on the microstructure and densification of iron powder," *Mater. Sci. Eng. A*, vol. 359, pp. 119–128, 2003.

[30] N. Read, W. Wang, K. Essa, and M. M. Attallah, "Selective laser melting of AlSi10Mg alloy: Process optimisation and mechanical properties development," *Mater. Des.*, vol. 65, pp. 417–424, 2015.

[31] J. R. Davis, *Stainless Steels*. Materials Park, Ohio : ASM International, 1994.

[32] A. A. Ramadan, R. D. Gould, and A. Ashour, "On the Van der Pauw method of resistivity measurements," *Thin Solid Films*, vol. 239, no. 2, pp. 272–275, 1994.

[33] K. Szymański, K. Łapiński, and J. L. Cieśliński, "Determination of the Riemann modulus and sheet resistance of a sample with a hole by the van der Pauw method," *Meas. Sci. Technol.*, vol. 26, no. 5, p. 055003, 2015.

[34] J. G. Webster, *Electrical Measurement, Signal Processing and Displays*. CRC Press, 2004.

[35] E. Yasa and J. P. Kruth, "Application of Laser Re-Melting on Selective Laser Melting Parts," *Adv. Prod. Eng. Manag.*, vol. 6, no. 4, pp. 259–270, 2011.

[36] E. Yasa and J.-P. Kruth, "Microstructural investigation of Selective Laser Melting 316L stainless steel parts exposed to laser re-melting," *Procedia Eng.*, vol. 19, pp. 389–395, 2011.

[37] J. A. Cherry, H. M. Davies, S. Mehmood, N. P. Lavery, S. G. R. Brown, and J. Sienz, "Investigation into the effect of process parameters on microstructural and physical properties of 316L stainless steel parts by selective laser melting," *Int. J. Adv. Manuf. Technol.*, vol. 76, no. 5–8, pp. 869–879, 2014.

[38] L. Dong, A. Makradi, S. Ahzi, and Y. Remond, "Three-dimensional transient finite element analysis of the selective laser sintering process," *J. Mater. Process. Technol.*, vol. 209, no. 2, pp. 700–706, 2009.

[39] W. Zhu, C. Yan, Y. Shi, S. Wen, J. Liu, and Y. Shi, "Investigation into mechanical and microstructural properties of polypropylene manufactured by selective laser sintering in comparison with injection molding counterparts," *Mater. Des.*, vol. 82, pp. 37–45, 2015.

[40] M. Averyanova, P. Bertrand, and B. Verquin, "Studying the influence of initial powder characteristics on the properties of final parts manufactured by the selective laser melting technology," *Virtual Phys. Prototyp.*, vol. 6, no. 4, pp. 215–223, 2011.

[41] E. Yasa, J. Deckers, and J. Kruth, "The investigation of the influence of laser re-melting on density, surface quality and microstructure of selective laser melting parts," *Rapid Prototyp. J.*, vol. 17, no. 5, pp. 312–327, 2011.

[42] C. S. Wright, K. W. Dalgarno, and M. M. Dewidar, "Processing conditions and mechanical properties of high speed steel parts fabricated using direct selective laser sintering," *J. Eng. Manuf.*, vol. 217, pp. 1651–1663, 2009.

[43] J. Jhabvala, E. Boillat, T. Antignac, and R. Glardon, "On the effect of scanning strategies in the selective laser melting process," *Virtual Phys. Prototyp.*, vol. 5, no. 2, pp. 99–109, 2010.

[44] R. Mahshid, H. N. Hansen, and K. L. Højbjerre, "Strength analysis and modeling of cellular lattice structures manufactured using selective laser melting for tooling applications," *Mater. Des.*, 2016.

[45] T. B. Sercombe, X. Xu, V. J. Challis, R. Green, S. Yue, Z. Zhang, and P. D. Lee, "Failure modes in high strength and stiffness to weight scaffolds produced by Selective Laser Melting," *Mater. Des.*, vol. 67, pp. 501–508, 2015.

[46] A. Simchi, H. Danninger, and B. Weiss, "Microstructural modelling of electrical conductivity and mechanical properties of sintered ferrous materials," *Powder Metall.*, vol. 43, no. 3, pp. 219–227, 2000.

[47] J. M. Montes, F. G. Cuevas, and J. Cintas, "Porosity effect on the electrical conductivity of sintered powder compacts," *Appl. Phys. A*, vol. 92, no. 2, pp. 375–380, 2008.

[48] J.-P. Kruth, P. Mercelis, J. Van Vaerenbergh, L. Froyen, and M. Rombouts, "Binding mechanisms in selective laser sintering and selective laser melting," *Rapid Prototyp. J.*, vol. 11, no. 1, pp. 26–36, 2005.

[49] N. K. Tolochko, M. K. Arshinov, A. V. Gusarov, V. I. Titov, T. Laoui, and L. Froyen, "Mechanisms of selective laser sintering and heat transfer in Ti powder," *Rapid Prototyp. J.*, vol. 9, no. 5, pp. 314–326, 2003.

[50] M. Ni, M. K. H. Leung, D. Y. C. Leung, and K. Sumathy, "A review and recent developments in photocatalytic water-splitting using TiO2 for hydrogen production," *Renew. Sustain. Energy Rev.*, vol. 11, no. 3, pp. 401–425, 2007.

[51] L. C. R. Schneider, C. L. Martin, Y. Bultel, L. Dessemond, and D. Bouvard, "Percolation effects in functionally graded SOFC electrodes," *Electrochim. Acta*, vol. 52, no. 9, pp. 3190–3198, 2007.